A micromechanics-based enhanced plastic damage model including localization analysis for heterogeneous geomaterials

Wanqing Shen, Jian-Fu Shao, Y.J. Cao, S.S. Wang, W.Y. Xu

Version of Record: https://www.sciencedirect.com/science/article/pii/S0266352X20300756
Manuscript_b7d21f4573dd047e7cff03b2caa451e9

A micromechanics-based enhanced plastic damage model including localization analysis for heterogeneous geomaterials

W.Q. Shen[a,b], J.F. Shao[a,b,*], Y.J. Cao[a], S.S. Wang[a], W.Y. Xu[a]

[a] *College of Civil and Transportation Engineering, Hohai University, Nanjing, China*
[b] *Univ. Lille, CNRS, Centrale Lille, FRE 2016 - LaMcube - Laboratoire de Mécanique Multiphysique et Multiéchelle, F-59000, Lille, Fracne*

Abstract

A micromechanics-based plastic damage model including localised failure is proposed in the present work for heterogenous materials which can be treated as a porous matrix reinforced by mineral inclusions. This model explicitly considers the influences of pores and inclusions volume fractions, also the solid phase dilatancy on the overall mechanical performance. The induced damage in solid phase is also considered. Based on this two-scale model, the bifurcation analysis is performed to detect both the onset and orientation of localization band. Numerical simulations are carried out for different cases. It is found that the material's microstructure affects importantly the onset point of the localization and the post-localization behavior. As an example of validation, the proposed model enhanced with localization analysis is then adopted to predict the overall mechanical response before and post localization of this typical claystone. Comparing with the experimental results, the capacity of this enhanced modelling is clearly demonstrated.

Keywords: Micromechanical models, Localization analysis, Plastic deformation, Damage, Porous materials, Claystone

1. Introduction

In many engineering applications (like nuclear waste storage, mining engineering, etc.), rock and cement-based material are the most studied materials for the safety and durability [19, 37, 41, 10, 2, 35]. In the context of the radioactive waste storage, the Callovo-Oxfordian

*Corresponding author
Email address: Jian-Fu.Shao@polytech-lille.fr (J.F. Shao)

(COx) claystone has been chosen as a possible natural protection of the radioactive waste disposal in French [8, 40, 3]. These materials are generally heterogeneous with complex microstructures which affect their overall mechanical performance. Many constitutive modellings were established for describing the mechanical response of such materials. For example, [9, 42, 20] have developed phenomenological models for the COx claystone. These models are essentially generally formulated and calibrated from macroscopic laboratory tests. The material's microstructural information is not explicitly taken into account. For instance, experimental results indicates that the material strength is affected by the volume fraction of pore and mineral compositions [8, 40, 3]. To overcome these weaknesses, many researchers focus on the micromechanics-based constitutive modelings by using the up-scaling approach. Based on the pioneer's work [17] for a hollow sphere with a pressure independent matrix (von Mises type), a high number of strength criteria have been formulated for different kinds of porous materials. For example, some authors have considered effects of pore size and spatial distribution at different scales [25, 12, 7, 29, 58, 59, 47, 44, 51, 43]; others have studied the void shape effects [14, 15, 22, 26, 27, 46]. Different matrix properties have been investigated: Mises-Schleicher type matrix [23, 11, 28, 56, 54], Green type one [47, 48, 52, 51, 55, 53] and Drucker-Prager type one [21, 4, 16, 24, 57, 44, 11, 49] have also been investigated. On the other hand, some studies have focused on the effects of mineral grains in heterogeneous materials. Macroscopic strength criteria have been derived in [13, 5, 24, 6]. What's more, the Hill's incremental approach is adopted in [1, 48] by including both effects of mineral grains and pores on the macroscopic behaviors of COx claystone. With two-step homogenization procedures, some authors [45, 18, 6] have even proposed analytical elastic-plastic modelings which simultaneously consider the meso-inclusions and micro-porosity.

However, in most previous studies, only elastic-plastic deformations are investigated. The progressive failure due to onset of localized bands has not been taken into account. Indeed, in most experimental studies [8, 40, 3], it is found that a single or multiple localized cracks are formed after the peak stress in laboratory tests. The stress and strain fields in tested samples are no more uniform after the onset of localization. The orientation of localized zones (shear band or compaction band) depends on loading paths [36]. The description of localization is a crucial issue for the analysis of failure process and excavation induced damaged and fractured zones. Recently, the localised failure processes of sandstone have

been investigated by some interesting studies [34, 32, 33] by using an enhanced macroscopic constitutive model including the analysis of localization onset and post-localization behavior.

In this work, we focus on the analysis of localization phenomena in heterogenous rock-like materials by developing an enhanced micromechanicas-based elastic-plastic damage model. As a novelty, we shall investigate the influences of micro-structures (pores and mineral inclusions) on the onset of localized bands and on the post-localization behavior of such materials.

There are five principal parts in this work: adopting the macroscopic strength criterion issued from nonlinear homogenization procedure [50], a basic constitutive modelling is presented in section 2 for heterogeneous materials with micro porosity and meso inclusions. This basic model is enhanced in section 3 by including the analysis of localization onset and post-localization response. Then, it is fully studied in section 4, especially by considering the influences of microstructure parameters on the localised failure process. Finally, an application is carried out in section 5 to study both the pre- and post- localization behaviors of COx claystone, with different material composition and different loading condition.

2. Micromechanics-based constitutive model with microstructural information

In this section, a micromechanics-based elastic-plastic damage modelling is firstly proposed to predict the macroscopic strength of heterogeneous materials with effects of porosity, mineral grains and the dilatation of the solid phase. Figure 1 shows the representative volume element (RVE) of the studied heterogeneous material. At the mesoscopic scale, the inclusions are embedded in a matrix which is a porous medium at the microscopic scale. The pores and inclusions are both assumed to be spherical. In the RVE, the total domain is denoted as V, the ones occupied by the inclusion, the pore and the solid phase are given as: V_i, V_p and V_m, respectively. With these definitions, the micro-porosity at the microscopic scale and the volume fraction of inclusion at the mesoscopic scale can be calculated:

$$f = \frac{V_p}{V_p + V_m}, \qquad \rho = \frac{V_i}{V_i + V_m + V_p} \tag{1}$$

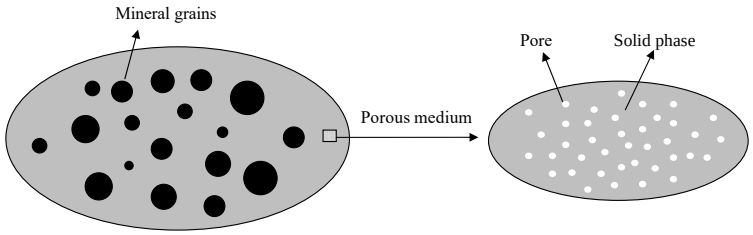

Figure 1: Heterogeneous material with micro-porosity and meso-inclusions

With the elastic loading, we consider firstly the porous medium at the microscopic scale. The effective elastic bulk moduli κ_{pm} and the shear one κ_{pm} of the porous medium depend on the local ones of the solid phase (κ_s, μ_s) and also the local volume fraction of pore f. Due to the spherical form, the Mori-Tanaka solution [30] is adopted here:

$$\kappa_{pm} = \frac{4(1-f)\kappa_s\mu_s}{4\mu_s + 3f\kappa_s}; \quad \mu_{pm} = \frac{(1-f)\mu_s}{1 + 6f\dfrac{\kappa_s + 2\mu^s}{9\kappa_s + 8\mu_s}} \tag{2}$$

At the macroscopic scale, the overall elastic properties κ^{hom}, μ^{hom} can be calculated by using the same homogenization procedure (2), considering the inclusion volume fraction ρ and the values of κ_{pm}, μ_{pm} obtained in the first up-scaling for porous medium.

The meso-inclusions are elastic, while the solid phase is elastoplastic and is described by the following Drucker-Prager model:

$$\Phi^m(\boldsymbol{\sigma}^s) = \sigma_d^s + \alpha(\sigma_m^s - \sigma_0) \leq 0 \tag{3}$$

where $\sigma_m^s = \mathrm{tr}\boldsymbol{\sigma}^s/3$, $\sigma_d^s = \sqrt{\boldsymbol{\sigma}^{s\prime} : \boldsymbol{\sigma}^{s\prime}}$ as a function of deviatoric part ($\boldsymbol{\sigma}^{s\prime} = \boldsymbol{\sigma}^s - \sigma_m^s\mathbf{1}$) of the local solid phase stress $\boldsymbol{\sigma}^s$. The stress in porous medium is defined as $\tilde{\boldsymbol{\sigma}}$. $\boldsymbol{\sigma}$ is the overall stress of the composite. α and σ_0 are material parameters, the frictional coefficient and the strength in the case of purely shear loading, respectively.

Based on the material's microstructure, a two-step up-scaling is adopted for the overall yield function. The micro-porosity f and the matrix's dilatation at the microscopic scale is considered in the first homogenization. The yield criterion obtained in [24] is adopted here to describe the effective response of this porous medium:

$$F^{mp}(\tilde{\boldsymbol{\sigma}}, f, \alpha) = \frac{1 + 2f/3}{\alpha^2}\tilde{\sigma}_d^2 + \left(\frac{3f}{2\alpha^2} - 1\right)\tilde{\sigma}_m^2 + 2(1-f)\sigma_0\tilde{\sigma}_m - (1-f)^2\sigma_0^2 = 0 \tag{4}$$

Considering the normality rule, the support function of the porous matrix can be calculated according to (4):

$$\pi^{mp} = (1-f)\sigma_0 \sqrt{\frac{3f}{3f-2\alpha^2}\frac{\alpha^2}{1+2f/3}}\sqrt{d_d^2 + \frac{1+2f/3}{3f/2-\alpha^2}d_v^2} - (1-f)\sigma_0\frac{2\alpha^2}{3f-2\alpha^2}d_v \qquad (5)$$

in which $\boldsymbol{d}$ denotes the strain rate, $d_v = \mathrm{tr}\boldsymbol{d}$, $d_d = \sqrt{\boldsymbol{d}' : \boldsymbol{d}'}$ with $\boldsymbol{d}' = \boldsymbol{d} - d_m\mathbf{1}$.

It is interesting to note that both the plastically dilatant and contractant behaviors can be observed even with the normality rule for the porous matrix. Differently from the Drucker-Prager criterion (3) of the solid phase at the microscopic scale (black line in Figure 2), the yield criterion (4) with the influence of porosity gives a closed surface as indicated by the illustrated blue lines. The dilatant and contractant behaviours can be predicted by this same yield surface, depending on the loading path and material microstructure information. For example, in the case with a porosity of $f = 0.1$, the plastic dilatancy can be obtained with a low confining pressure (green dashed line) while the contractancy can be observed with a high confining pressure (yellow dashed line). The porosity also has a great influence on the dilatant and contractant responses of porous material with the same loading condition. For example, following the triaxial compression test with a 2 MPa confining pressure (red dashed line), the porous matrix is plastically dilatant for the porosity $f = 0.1$. Inversely, it has a contractant behaviour when the porosity is $f = 0.35$. Taking into account the microstructure effect is the main advantage of micro-mechanical model comparing with the traditional phenomenological models.

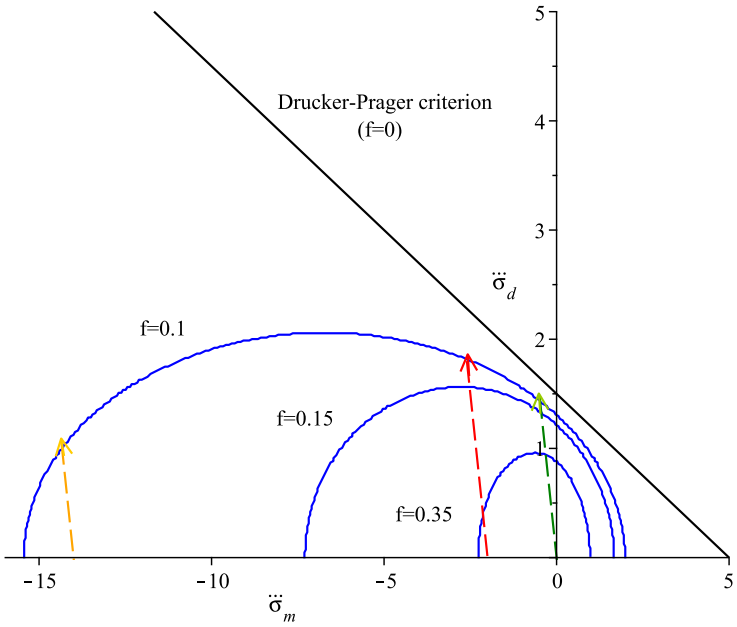

Figure 2: Yield surfaces predicted by criterion (4) with different porosity and different loading path, $\alpha = 0.3$, $\sigma_0 = 5$.

According the equation (5), the relations between the stress and strain can be expression as follows:

$$\begin{aligned} &\tilde{\boldsymbol{\sigma}} = \frac{\partial \pi^{mp}}{\partial \boldsymbol{d}} = 2\mu^{mp}\boldsymbol{d}' + \kappa^{mp} d_v \mathbf{1} + \sigma^p \mathbf{1}, \qquad \kappa^{mp} = \frac{1+2f/3}{3f/2-\alpha^2}\frac{N}{M}, \qquad 2\mu^{mp} = \frac{N}{M}, \\ &\tilde{\sigma}^p = -(1-f)\sigma_0 \frac{2\alpha^2}{3f-2\alpha^2}, \qquad M = \sqrt{d_d^2 + \frac{1+2f/3}{3f/2-\alpha^2} d_v^2}, \qquad N = (1-f)\sigma_0 \sqrt{\frac{3f}{3f-2\alpha^2}\frac{\alpha^2}{1+2f/3}} \end{aligned} \tag{6}$$

Based on the effective behavior of porous matrix, the influence of inclusion volume fraction on the macroscopic elastoplastic properties will be accounted in the second up-scaling. By adopting the modified secant method, [50] established a strength function for the studied material considering simultaneously the effects of f, ρ and and the dilatation property α of the solid phase, as illustrated in Figure 1. Here we take the main results and more details can be found in [50] for the derivation.

$$\Phi(\boldsymbol{\sigma}, f, \rho, \alpha) = \Theta\sigma_d^2 + \left(\frac{3f}{2\alpha^2} - 1\right)\sigma_m^2 + 2(1-f)\sigma_0\sigma_m - \frac{3+2f+3f\rho}{3+2f}(1-f)^2\sigma_0^2 = 0 \tag{7}$$

where $\Theta = \dfrac{\frac{1+2f/3}{\alpha^2} + \frac{2}{3}\rho\left(\frac{3f}{2\alpha^2} - 1\right)}{\frac{4\alpha^2-12f-9}{6\alpha^2-13f-6}\rho + 1}$.

For the purpose to consider the plastic hardening phenomena observed in the experimental and to construct a complete constitutive modelling, the frictional parameter α at the microscopic scale is chosen here as the plastic hardening law, which is a function of equivalent plastic strain ε_{eq}^{p} in the solid phase:

$$\bar{\alpha} = \alpha_m - (\alpha_m - \alpha_0)e^{-b_1\varepsilon_{eq}^{p}} \tag{8}$$

Then the yield function (7) can be rewritten as follows:

$$\Phi(\boldsymbol{\sigma}, f, \rho, \bar{\alpha}) = \Theta\sigma_d^2 + \left(\frac{3f}{2\bar{\alpha}^2} - 1\right)\sigma_m^2 + 2(1-f)\sigma_0\sigma_m - \frac{3+2f+3f\rho}{3+2f}(1-f)^2\sigma_0^2 = 0 \tag{9}$$

where $\Theta = \dfrac{\frac{1+2f/3}{\bar{\alpha}^2} + \frac{2}{3}\rho\left(\frac{3f}{2\bar{\alpha}^2} - 1\right)}{\frac{4\bar{\alpha}^2-12f-9}{6\bar{\alpha}^2-13f-6}\rho + 1}$.

For a general case, a non-associated flow rule is chosen in this constitutive modelling. Based on the yield criterion (9), a macroscopic plastic potential is introduced which depends on the microstructural information (f, ρ, $\bar{\alpha}$, $\bar{\beta}$ and σ_0):

$$G(\boldsymbol{\sigma}, f, \rho, \bar{\alpha}, \bar{\beta}) = \bar{\Theta}\sigma_d^2 + \left(\frac{3f}{2\bar{\alpha}\bar{\beta}} - 1\right)\sigma_m^2 + 2(1-f)\sigma_0\sigma_m - \frac{3+2f+3f\rho}{3+2f}(1-f)^2\sigma_0^2 \tag{10}$$

where $\bar{\Theta} = \dfrac{\frac{1+2f/3}{\bar{\alpha}\bar{\beta}} + \frac{2}{3}\rho\left(\frac{3f}{2\bar{\alpha}\bar{\beta}} - 1\right)}{\frac{4\bar{\alpha}\bar{\beta}-12f-9}{6\bar{\alpha}\bar{\beta}-13f-6}\rho + 1}$. $\bar{\beta}$ denotes the dilatancy parameter which controls the volumetric deformation. Similar to the plastic hardening law (8), $\bar{\beta}$ is chosen as function of ε_{eq}^{p}:

$$\bar{\beta} = \beta_m - (\beta_m - \beta_0)e^{-b_2\varepsilon_{eq}^{p}} \tag{11}$$

Based on the plastic potential (10), the macroscopic plastic deformation can be computed:

$$\boldsymbol{D}^{p} = \dot{\lambda}\frac{\partial G}{\partial \boldsymbol{\sigma}}(\boldsymbol{\sigma}, f, \rho, \bar{\alpha}, \bar{\beta}) \tag{12}$$

With the process of loading, the solid phase can be damaged because of the micro-cracks generations. This may be at the origin of macroscopic materials softening. For the simplicity, this softening effect will be considered by the degradation of the cohesion coefficient σ_0 in local criterion (3) of the solid phase:

$$\sigma_0 = c_0 + c_1 e^{-b_3<\varepsilon_{eq}^{p} - \varepsilon_r^{p}>} \tag{13}$$

where c_0 is the residual resistance of the solid phase; $< x - x_0 >$ is a mathematical operator which is 0 when $x \leq x_0$, otherwise $x - x_0$; ε_r^p is the reference values which controls the beginning of softening. For the simplicity, the equivalent plastic deformation at the microscopic scale will be taken as the reference value. In order to consider the microstructure effect and loading influence, this value is related to the macroscopic strain and the ratio of incremental values $\dot{E}_{eq}^p/\dot{E}_{eq}$ is chosen as the critical point. In this work, the value $\dot{E}_{eq}^p/\dot{E}_{eq} = 0.98$ is taken as the beginning of softening.

Based on (12), the local equivalent plastic strain can be computed:

$$\dot{\varepsilon}^p = \frac{\boldsymbol{\sigma} : \boldsymbol{D}^p}{(1-f)(1-\rho)\left[\bar{\alpha}\sigma_0 + (\bar{\beta} - \bar{\alpha})\frac{\sigma_m}{1-f}\right]} \tag{14}$$

The variations of pore and inclusion volume fractions are determined as:

$$\dot{f} = \frac{1-f}{1-\rho}\mathrm{tr}\mathbf{D}^p - (1-f)\bar{\beta}\dot{\varepsilon}_{eq}^p, \qquad \dot{\rho} = -\rho\mathrm{tr}\mathbf{D}^p \tag{15}$$

The plastic multiplier $\dot{\lambda}$ used in (12) can be fixed with the help of consistency condition:

$$\dot{\lambda} = \frac{\frac{\partial\Phi}{\partial\boldsymbol{\sigma}} : \mathbb{C} : \mathbf{D}}{\frac{\partial\Phi}{\partial\boldsymbol{\sigma}} : \mathbb{C} : \frac{\partial G}{\partial\boldsymbol{\sigma}} - \frac{\partial\Phi}{\partial f}\left[\frac{1-f}{1-\rho}\frac{\partial G}{\partial\sigma_m} - \bar{\beta}(1-f)Z\right] - \frac{\partial\Phi}{\partial\rho}(-\rho\frac{\partial G}{\partial\sigma_m}) - \frac{\partial\Phi}{\partial\bar{\alpha}}\frac{\partial\bar{\alpha}}{\partial\varepsilon_{eq}^p}Z - \frac{\partial\Phi}{\partial\sigma_0}\frac{\partial\sigma_0}{\partial\varepsilon_{eq}^p}Z} \tag{16}$$

where $Z = \frac{\boldsymbol{\sigma} : \frac{\partial G}{\partial\boldsymbol{\sigma}}}{(1-f)(1-\rho)\left(\bar{\alpha}\sigma_0 + (\bar{\beta}-\bar{\alpha})\frac{\sigma_m}{1-f}\right)}$, $\mathbb{C}$ is a fourth order elastic stiffness tensor which depends on material's microstructure (porosity f, inclusion volume fraction ρ) as shown in equation (2).

In the elastoplastic case, the tangent one $\mathbb{C}^{tan}$ of the studied material can be calculated:

$$\mathbb{C}^{tan} = \begin{cases} \mathbb{C} & \text{if} \quad \Phi(\boldsymbol{\sigma}, f, \rho, \bar{\alpha}) \leq 0, \quad \dot{\Phi}(\boldsymbol{\sigma}, f, \rho, \bar{\alpha}) < 0 \\ \mathbb{C} - \dfrac{\mathbb{C} : \frac{\partial G}{\partial\boldsymbol{\sigma}} \otimes \frac{\partial\Phi}{\partial\boldsymbol{\sigma}} : \mathbb{C}}{H^L} & \text{if} \quad \Phi(\boldsymbol{\sigma}, f, \rho, \bar{\alpha}) = 0, \quad \dot{\Phi}(\boldsymbol{\sigma}, f, \rho, \bar{\alpha}) = 0 \end{cases} \tag{17}$$

with $H^L = \frac{\partial\Phi}{\partial\boldsymbol{\sigma}} : \mathbb{C} : \frac{\partial G}{\partial\boldsymbol{\sigma}} - \frac{\partial\Phi}{\partial f}\left[\frac{1-f}{1-\rho}\frac{\partial G}{\partial\sigma_m} - \bar{\beta}(1-f)Z\right] - \frac{\partial\Phi}{\partial\rho}(-\rho\frac{\partial G}{\partial\sigma_m}) - \frac{\partial\Phi}{\partial\bar{\alpha}}\frac{\partial\bar{\alpha}}{\partial\varepsilon_{eq}^p}Z - \frac{\partial\Phi}{\partial\sigma_0}\frac{\partial\sigma_0}{\partial\varepsilon_{eq}^p}Z.$

This proposed multiscale constitutive model now is adopted to predict the overall mechanical behavior of heterogeneous materials as illustrated in Figure 1. The material's microstructure informations are explicitly and simultaneously accounted by this micromechanics based model, for example, volume fractions of pore and inclusion (f, ρ), also the dilatation α of solid phase. At the constitutive level, the studied material is homogeneous and the heterogeneous properties are directly considered in the criterion (9) and the plastic potential (10). The prediction is well adopted before the peak strength of the material. The post-peak behavior will accounted in the following section due to the localization zone.

3. Analysis of localization onset and post-localization behavior

3.1. Onset condition of the localization band

At the beginning of the loading, the material is assumed as homogeneous and its mechanical behavior is described by the micromechanics based model presented in section 2. With the loading process, the material may loss is stability and the discontinuous bifurcation will be generated. To predict the localization effects on macroscopic behaviors of the studied heterogeneous materials through this micro-macro constitutive model, one need to specify its onset and orientation. For this purpose, the classical method for the determination of discontinuous bifurcation is adopted in this study as in [34]. We first present the acoustic tensor $\mathbf{A}$ which can be expressed as $\mathbf{A} = \underline{n} \cdot \mathbb{C}^{tan} \cdot \underline{n}$, in which $\mathbb{C}^{tan}$ is the tangent stiffness and calculated in the above constitutive model by the equation (17); $\underline{n}$ is the unit direction vector. As illustrated in the Figure 3, here $\underline{n}$ is the direction of the localization band. In spherical coordinate, $\underline{n}$ is given as:

$$\underline{n} = [n_1, n_2, n_3]^t = [\sin\theta\sin\varphi,\ \sin\theta\cos\varphi,\ \cos\theta]^t \tag{18}$$

According to the symmetric property, the φ is taken as $90°$; the range of θ is $[-90°, 90°]$.

The beginning of localization is fixed at the point when the definiteness of this acoustic tensor $\mathbf{A}$ becomes negative:

$$\det(\mathbf{A}) \leq 0 \tag{19}$$

With the loading path, the first stress-strain state for which $\det(\mathbf{A}) \leq 0$ is checked to fix the bifurcation inception. According to the $\mathbb{C}^{tan}$ given by (17), the value of $\det(\mathbf{A})$ can be calculated by scanning all the possible directions $\underline{n}$. Once one gets $\det(\mathbf{A}) \leq 0$, usually a range of orientation $\underline{n}$ can be mathematically found to satisfy the onset condition and any $\underline{n}$ in this range is a possible direction of the localization band. In this work, the direction which makes the minimum value of $\det(\mathbf{A})$ in the domain $\det(\mathbf{A}) \leq 0$ is chosen as the most probable band orientation and adopted in the following loading process.

3.2. Post-localization behavior

After this beginning of localization band, the studied material will be no longer homogeneous. There are two principal parts in the studied volume: the localization zone and the

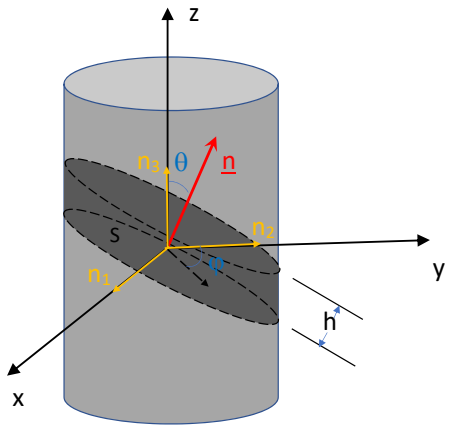

Figure 3: The orientation of the Localization zone

outside one. In this case, the traditional constitutive models can not be used directly to describe its macroscopic mechanical behaviors. These models should be improved or extended to detect the onset of localization zone and to take into account the macroscopic behaviors of post-localization. As illustrated in Figure 3, one need to separated well this two phases: inside and outside localization zone. h is the thickness of the localization zone. According to the average area S of the localization zone's surface and the total volume Ω, the content of this zone is calculated : $\phi = \frac{hS}{\Omega}$. The width of the localisation band depends on both microstructure of the studied material and also the loading conditions. With the process of loading, it will also change during the deformation. For the simplicity, the localization band thickness here is treated as a material property and fixed throughout the failure process. At this step, the constitutive presented in the above section well be applied separately to describe the mechanical behaviors inside and outside the localization zone. To be clarity, σ_i and ε_i denote the stress and strain inside the localization zone while the outside ones are defined as σ_o and ε_o, respectively. The total ones at the macroscopic scale are defined as $\mathbf{\Sigma}$ and $\mathbf{E}$. The strain rate relation between $\dot{\mathbf{E}}$, $\dot{\varepsilon}_i$ and $\dot{\varepsilon}_o$ can be found:

$$\dot{\mathbf{E}} = \phi\dot{\varepsilon}_i + (1-\phi)\dot{\varepsilon}_o \tag{20}$$

Then, it is necessary to calculate the strain rate $\dot{\varepsilon}_i$ inside the localization zone. According

to the works of [31, 34, 32], it takes the following simple form:

$$\dot{\varepsilon}_i = \dot{\varepsilon}_o + \frac{1}{h}(\underline{n} \otimes [\underline{\dot{u}}])^s \tag{21}$$

According to (21), the tensor of strain rate is composed of two parts. The first part is the homogeneous strain rate. The second one is kinematically due to the discontinuous field of displacement rate, denoted as $[\underline{\dot{u}}]$, with $\underline{n}$ being the unit normal vector of the localization band. Therefore, unlike strain localization problems commonly studied by using the bifurcation theory, in this study, we consider crack-like localization problems in rock-like materials. There are displacement discontinuities crossing the localized band. However, it is assumed that this crack-like localization is generated by a progressive strain and micro-cracks localization process. It is a priori assumed that the classical bifurcation criterion can be still used for the detection of localization inception.

According equations (20) and (21), the local strain rates $\dot{\varepsilon}_i$ and $\dot{\varepsilon}_o$ can be derived as functions of the macroscopic one $\dot{\mathbf{E}}$ and $[\underline{\dot{u}}]$:

$$\dot{\varepsilon}_o = \dot{\mathbf{E}} - \frac{\phi}{h}(\underline{n} \otimes [\underline{\dot{u}}])^s, \qquad \dot{\varepsilon}_i = \dot{\mathbf{E}} + \frac{1-\phi}{h}(\underline{n} \otimes [\underline{\dot{u}}])^s \tag{22}$$

Based on the equilibration between the macroscopic work and the average value of local one, the following relation can be derived:

$$\mathbf{\Sigma} : \dot{\mathbf{E}} = \phi\sigma_i : \dot{\varepsilon}_i + (1-\phi)\sigma_o : \dot{\varepsilon}_o \tag{23}$$

Combining equations (20) (22) and (23), we obtain:

$$[\mathbf{\Sigma} - \phi\sigma_i - (1-\phi)\sigma_o] : \dot{\mathbf{E}} - \frac{\phi(1-\phi)}{h}(\sigma_i \cdot \underline{n} - \sigma_o \cdot \underline{n}) \cdot [\underline{\dot{u}}] = 0 \tag{24}$$

The equation (24) should be satisfied for any values of $[\underline{\dot{u}}]$ and $\dot{\mathbf{E}}$. With this condition, the following results can be derived [32]:

$$\begin{cases} \sigma_i \cdot \underline{n} = \sigma_o \cdot \underline{n}, \\ \mathbf{\Sigma} = \phi\sigma_i + (1-\phi)\sigma_o \end{cases} \tag{25}$$

The localization zone and the outside part are assumed to be homogeneous. By using the inside and outside tangent stiffness: $\mathbb{C}_i^{tan}$ and $\mathbb{C}_o^{tan}$, the local stress rate can be computed:

$\dot{\sigma}_i = \mathbb{C}_i^{tan} : \dot{\varepsilon}_i$, $\dot{\sigma}_o = \mathbb{C}_o^{tan} : \dot{\varepsilon}_o$. Considering the traction condition of equation (25), the velocity jump $[\underline{\dot{u}}]$ is given as:

$$\begin{aligned} &[\underline{\dot{u}}] = h\mathbf{B} \cdot \left(\mathbb{C}_o^{tan} - \mathbb{C}_i^{tan}\right) : \dot{\mathbf{E}} \cdot \underline{n}, \qquad \text{with} \\ &\mathbf{B} = \left[\phi\left(\underline{n} \cdot \mathbb{C}_o^{tan} \cdot \underline{n}\right) + (1-\phi)\left(\underline{n} \cdot \mathbb{C}_i^{tan} \cdot \underline{n}\right)\right]^{-1} \end{aligned} \tag{26}$$

Substituting the expression of $[\underline{\dot{u}}]$ in (22) and (25), the macroscopic tangent stiffness $\mathbb{C}_m^{tan}$ can be obtained ([32]):

$$\begin{aligned} &\dot{\mathbf{\Sigma}} = \mathbb{C}_m^{tan} : \dot{\mathbf{E}}, \qquad \text{with} \\ &\mathbb{C}_m^{tan} = \phi\mathbb{C}_i^{tan} + (1-\phi)\mathbb{C}_o^{tan} - \phi(1-\phi)\left(\mathbb{C}_o^{tan} - \mathbb{C}_i^{tan}\right) : \left[\underline{n} \otimes \mathbf{B} \cdot \left(\mathbb{C}_o^{tan} - \mathbb{C}_i^{tan}\right) \cdot \underline{n}\right] \end{aligned} \tag{27}$$

in which the macroscopic tangent stiffness $\mathbb{C}_m^{tan}$ reduces to the homogeneous one in the case of $\mathbb{C}_i^{tan} = \mathbb{C}_o^{tan}$.

Before the beginning of the bifurcation, the studied material is homogeneous. Its macroscopic mechanical behavior is described by this micromechanics-based constitutive modelling established in above section. According to the state of $\mathbb{C}^{tan}$ calculated by equation (17), the condition of the onset localization zone is checked. Once the equation (19) is satisfied, the studied material will be separated into two parts: the localization zone and the outside part. In each part, the sub-materials are homogeneous respectively. As assumed in [33, 34, 32], the zone outside the localization unloads elastically at the initial bifurcation while the inside behavior is inelastic. According to the distributions of the incremental loading $\dot{\mathbf{E}}$ for the zone inside ($\dot{\varepsilon}_i$) and outside ($\dot{\varepsilon}_o$) the localization zone, each part can exhibit either elastic or elastoplastic behavior which is determined separately by the proposed constitutive model. At this step, the inside and outside mechanical states are different and the corresponding plastic parameters in the constitutive model are conserved and updated separately. In the following section, this model will be fully studied.

4. Model's sensitivity study

The proposed micromechanics-based constitutive modelling is firstly implemented in Abaqus. As presented in [33], the implicit stress return algorithms are adopted here. The influences of parameter f, ρ, ϕ and b_3 on the localization zone and material's macroscopic performance will be emphatically studied. Table 1 shows the common parameters used in this constitutive model.

	Solid phase	Inclusion
Elastic	$E_s = 5GPa$	$E_i = 98GPa$
parameters	$v_s = 0.33$	$v_i = 0.15$
Plastic	$T_0 = 10^{-10}$, $T_m = 0.68$, $b_1 = b_2 = 200$	
parameters	$t_0 = -1.1$, $t_m = 0.3$, $c_0 = c_1 = 15$ Mpa	

Table 1: Common parameters used in the constitutive model.

Figure 4 illustrates the influence of f on overall behavior for the case of triaxial loading with 10 Mpa confining pressure. The inclusion content $\rho = 0.4$, the volume fraction of the localization zone $\phi = 0.2$ and $b_3 = 90$ in the softening rule. Different porosities are chosen: $f = 0.15, 0.25, 0.30$. The stress-strain curve are shown in Figure4-a. The material resistance decreases quickly as the increase of f. The performance of post-localization is also affected by f. According to the values of $\det(\mathbf{A})$ given in Figure 4-b, The porosity has an influence on the onset and orientation of localization band. The values of the inclined angle θ which makes the minimum $\det(\mathbf{A})$ are 49°, 46°, 45° for these three cases. The proposed model is able to predict the plastic shearing and pore collapse mechanism by the same yield surface. With the increase of porosity, there is a transition from shear band to compaction one. With the process of loading, the distributions of the axial deformation are shown in Figure 4-c. During time $0 \rightarrow 1$, the confining pressure is applied firstly, then the deviatoric loading is added in time $1 \rightarrow 2$. Before the point B, the material is homogeneous. The bifurcation begins at this point. For the case $f = 0.3$, the outside part is elastic while the inside one is elastoplastic. Due to the localization zone, the axial deformation increases quickly in the localization zone (dashed line). The same phenomena can be found for $f = 0.25$ and 0.15. With the same loading procedure and low porosity, the mechanical behavior becomes more complex. Combining the Figure 4-d of the local equivalent plastic deformation ε_{eq}^p evolution, one can find that the elastic behavior becomes inelastic one outside the localization zone after certain load, while the plastic deformation growth ratio decreases inside the zone. Due to the localization, the distributions of the incremental loading inside and outside the zone are total different. There is a sudden increase inside the localization zone. Based on

the mechanical behavior in each part, there is a sudden drop of material strength. The corresponding evolutions of f and ρ are illustrated on Figure 4-e and f, respectively. One can see that the evolutions of porosity are totally different inside and outside localization zone. The inside porosity are much smaller than the outside one because of the localization effects. The variation of ρ are complex but relatively small.

The effects of inclusion content ρ is investigated in Figure 5 with $f = 0.25$, other parameter are kept the same. According to the Figure 5-a, the inclusion content ρ increases the material strength. However, the value of $\det(\mathbf{A})$ shown in Figure 5-b indicates that the higher content of inclusion makes the material more unstable and the happens of bifurcation are more possible. Unlike the case of porosity, the inclusion content ρ affect importantly the onset localization zone, as the three point A, B and C given in the Figures 5-c and -d. With the process of loading, the porosity inside the zone decreases quickly after the point of bifurcation. Comparing with the porosity, the evolution of inclusion is small.

By taking $f = 0.25$ and $\rho = 0.4$, the influence of the localization band thickness ϕ is studied in Figure 6. Different values are considered as $\phi = 0.15$, 0.25, 0.35 and 0.45. We can see that its onset point and orientation have no relation with ϕ (Figure 6-b). But it affects the post-behavior. As shown in Figure 6-a of the stress-strain relation, the strength drop becomes more gradual with the increasing of ϕ, which means that the material is more homogeneous. The corresponding evolutions of the inside and outside axial deformations, the plastic equivalent deformations in the solid phase, the porosities and inclusion contents are illustrated in Figure 6-c to f.

The softening rule has an important influence on the localization failure analysis. The parameter b_3 in the softening rule affects the tangent stiffness $\mathbb{C}^{tan}$ (17). With the small values, for example $b_3 = 60$, the values of $\det(\mathbf{A})$ is positif for all directions θ and there is no bifurcation. So the studied material are homogeneous and the inside and outside evolutions of axial deformation, ε^p_{eq}, f and ρ are coincident (green lines). With the increasing of the value b_3, the material softening increases and it affects the localization procedure. When $b_3 = 90$, the material strength drop in the stress-strain curve are much sharper than the one of $b_3 = 70$ due to the localization zone. The same results can be found for the inside axial deformation and plastic equivalent deformation. The higher values of b_3 makes the more possibility of localization.

The effects of confining pressure on overall performance is investigated with $\rho = 0.4$, $f = 0.25$, $\phi = 0.2$, $b_3 = 90$. The material resistance increases with the increasing of confining pressure which has an important effect on the values of $\det(\mathbf{A})$ and affects the onset point of the localization zone, as illustrated in Figure 8. Concerning the post-localization behavior, the stress drop in the uniaxial loading is much more gradual than the one in triaxial loading.

In the following section, this multiscale constitutive modelling with the effect of localization will be used to predict the macroscopic performances of claystone with different material compositions and different confining pressure.

- Influence of porosity f

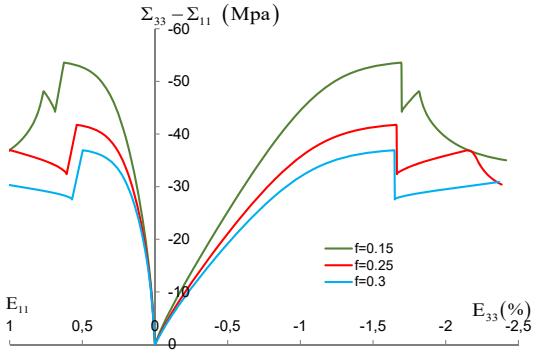

(a) Stress-strain relation

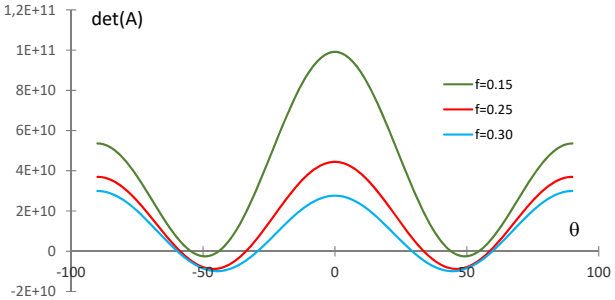

(b) det(**A**) as a function of localization band angle θ

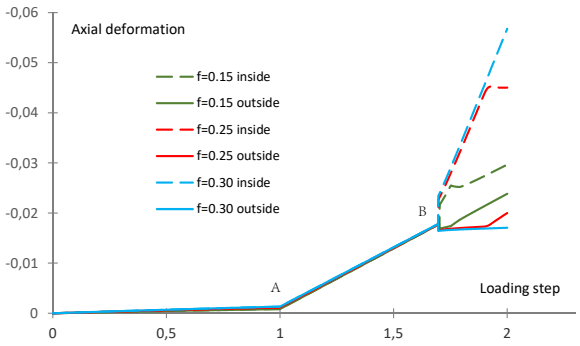

(c) Evolution of axial strain with loading step

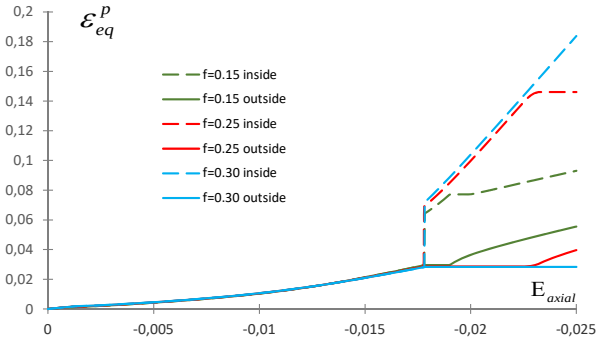

(d) Evolution of ε_{eq}^{p}

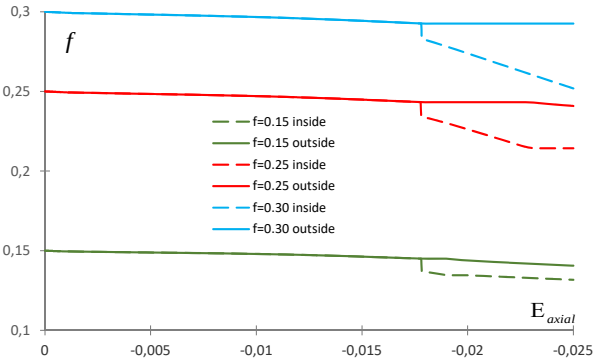

(e) Evolution of porosity f

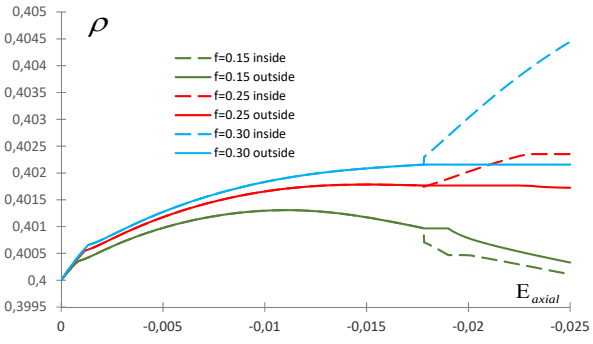

(f) Evolution of volume fraction of inclusion ρ

Figure 4: Influence of porosity f on the mechanical behaviors, $\rho = 0.4$, $Pc = 10$ Mpa, $b_3 = 90$, $\phi = 0.2$

- Influence of inclusion volume fraction ρ

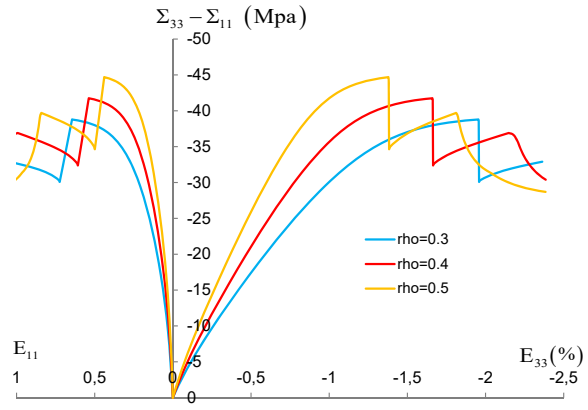

(a) Stress-strain relation

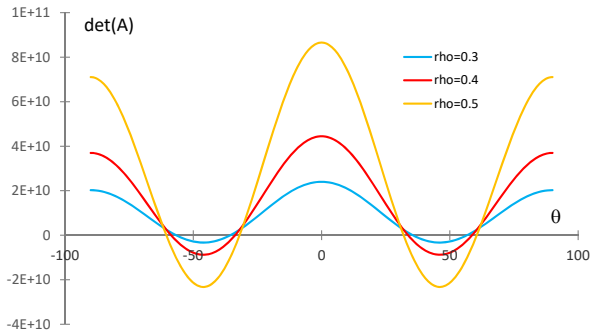

(b) det(**A**) as a function of localization band angle θ

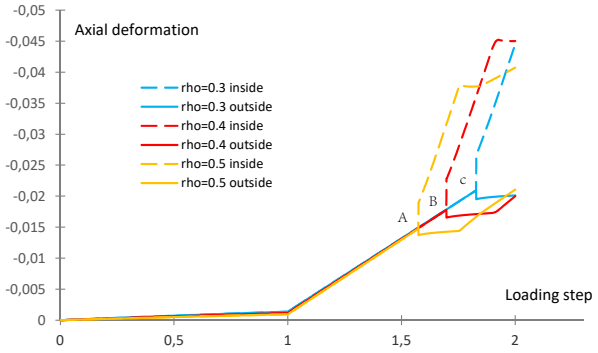

(c) Evolution of axial strain with loading step

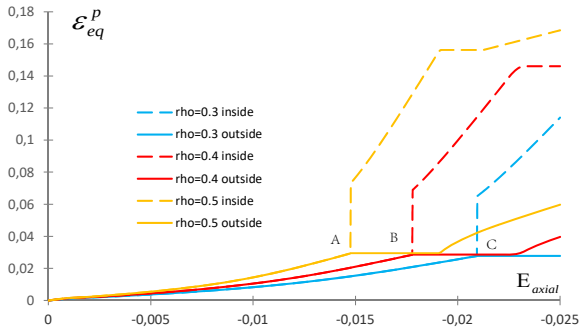

(d) Evolution of ε^p_{eq}

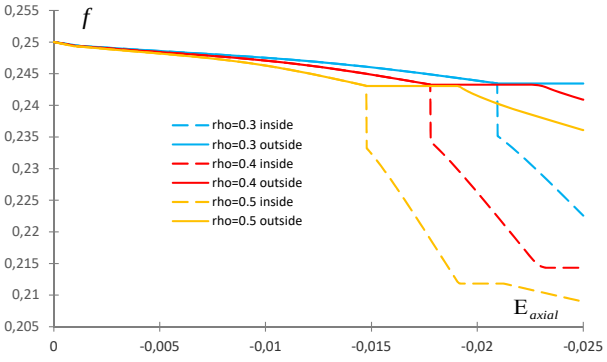

(e) Evolution of porosity f

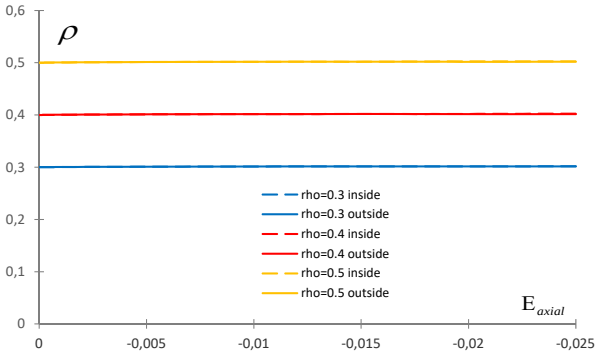

(f) Evolution of volume fraction of inclusion ρ

Figure 5: Influence of inclusion volume fraction ρ on the mechanical behaviors, $f = 0.25$, $Pc = 10$ Mpa, $b_3 = 90$, $\phi = 0.2$

- Influence of band volume fraction ϕ

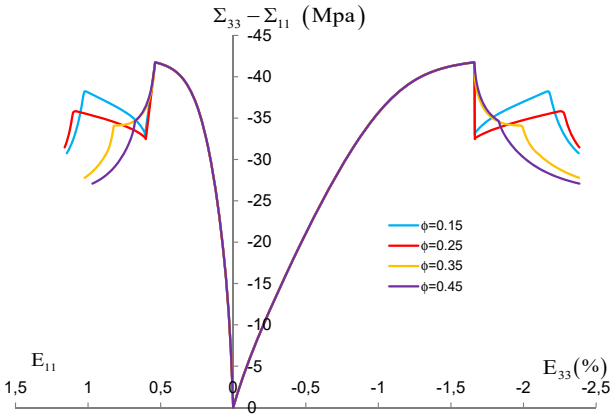

(a) Stress-strain relation

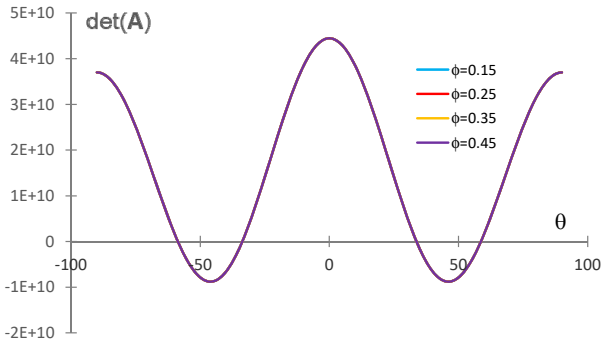

(b) det(**A**) as a function of localization band angle θ

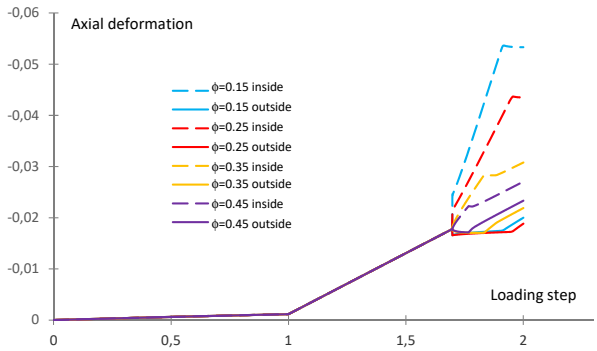

(c) Evolution of axial strain with loading step

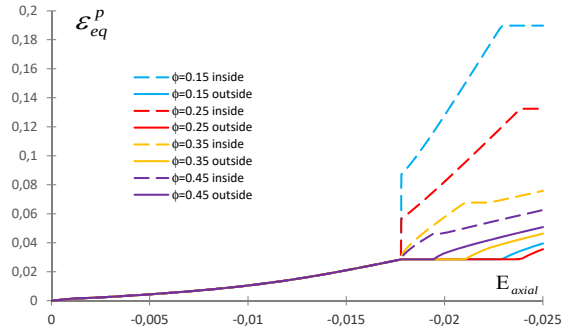

(d) Evolution of ε_{eq}^{p}

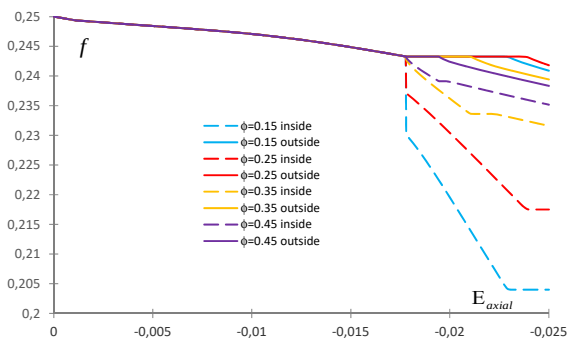

(e) Evolution of porosity f

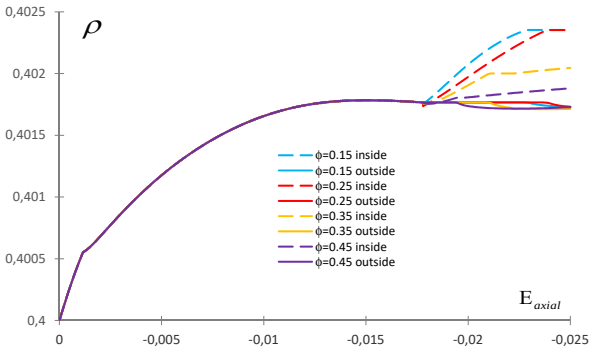

(f) Evolution of volume fraction of inclusion ρ

Figure 6: Influence of localization band size ϕ on the mechanical behaviors, $\rho = 0.4$, $f = 0.25$, $Pc = 10$ Mpa, $b_3 = 90$

- Influence of softening rule b_3

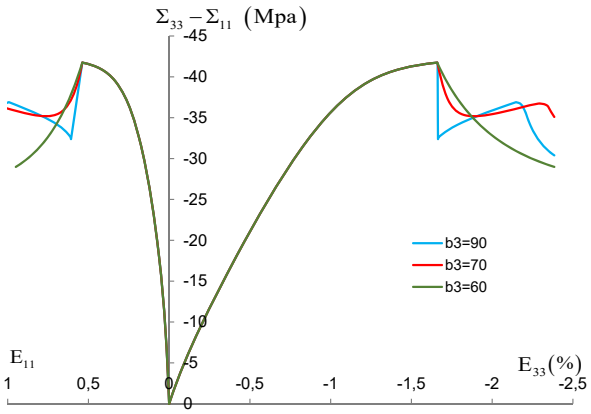

(a) Stress-strain relation

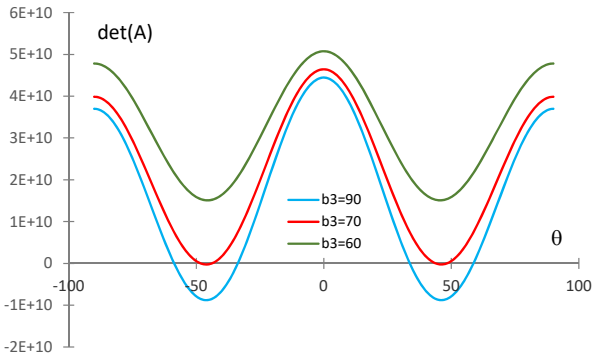

(b) det(**A**) as a function of localization band angle θ

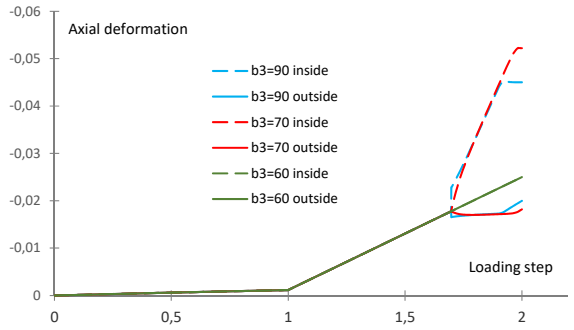

(c) Evolution of axial strain with loading step

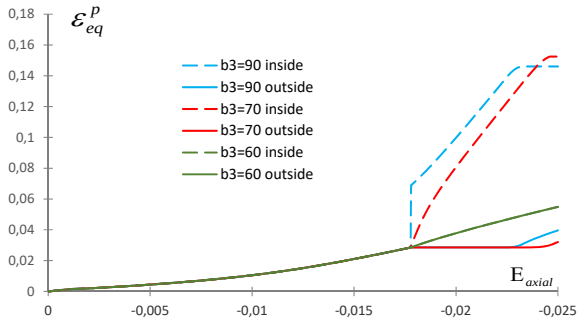

(d) Evolution of ε_{eq}^{p}

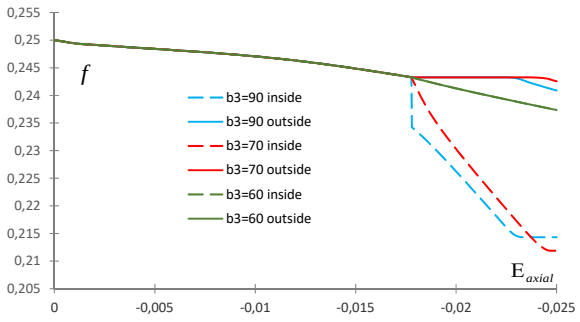

(e) Evolution of porosity f

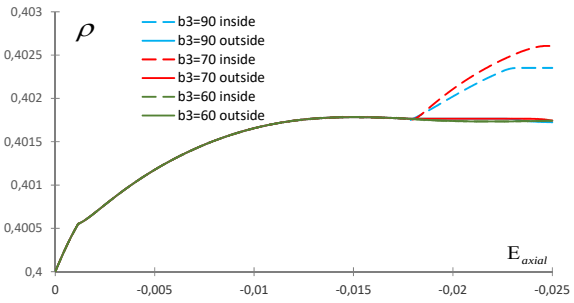

(f) Evolution of volume fraction of inclusion ρ

Figure 7: Influence of model parameter b_3 on the mechanical behaviors, $\rho = 0.4$, $f = 0.25$, $Pc = 10$ Mpa, $\phi = 0.2$

- Influence of confining pressure Pc

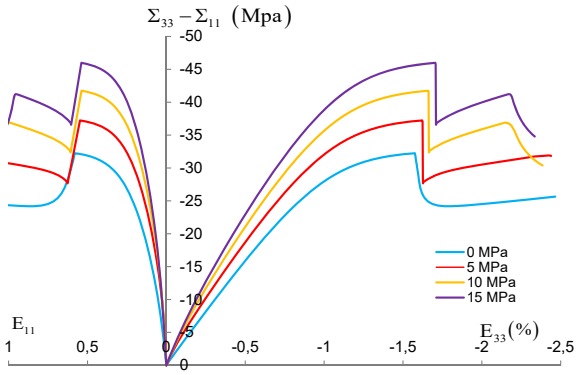

(a) Stress-strain relation

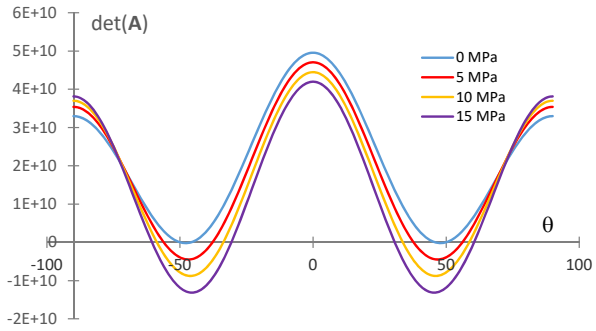

(b) det(**A**) as a function of localization band angle θ

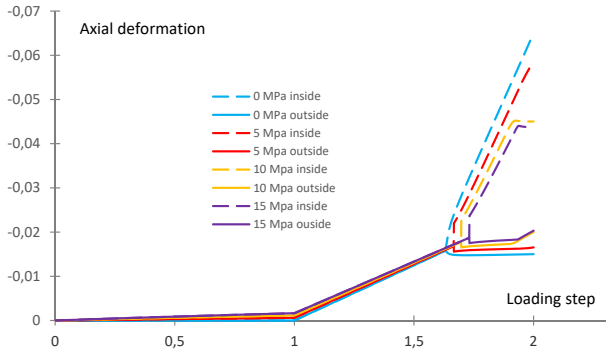

(c) Evolution of axial strain with loading step

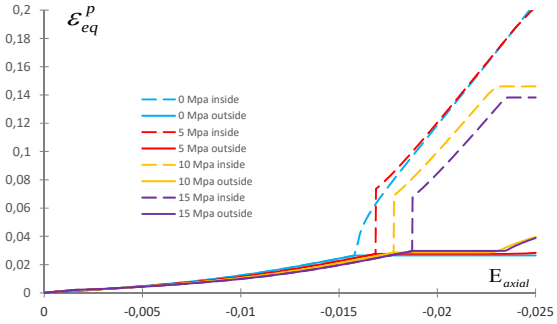

(d) Evolution of ε_{eq}^{p}

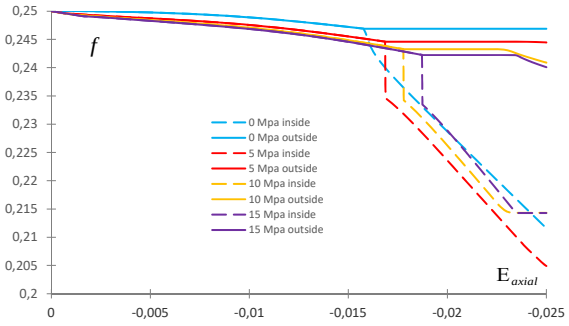

(e) Evolution of porosity f

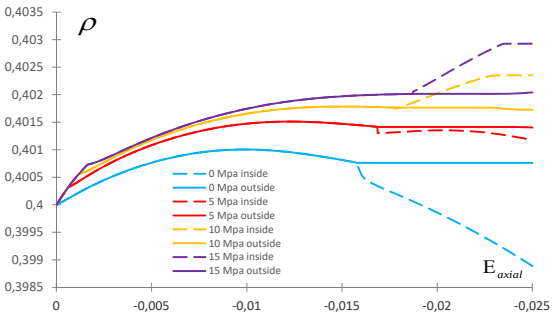

(f) Evolution of volume fraction of inclusion ρ

Figure 8: Confining pressure effect on the overall performance, $\rho = 0.4$, $f = 0.25$, $\phi = 0.2$, $b_3 = 90$

5. Application to Callovo-Oxfordian (COx) claystone

In the nuclear waste storage investigation, the layer of COx has been chosen as a possible geological disposal of radioactive wastes in French. Many experimental and theoretical investigations has been performed to better under stand this clayey rock. According to [40], the clay matrix is quasi continuous and reinforced essentially by quartz and calcite at the mesoscopic scale. Its composition varies with the depth. Generally, the clay has 40 to 50%, the volume fraction of calcite is about 20 to 27% and the one of quartz is from 23 to 25%. The average porosity is $11 \sim 14\%$ which mostly located in clay. Normally, initially anisotropy and damage induced anisotropy can be found in rock-like materials. Some works have been done for this point(such as [39, 38]). The purpose of this study is to study the localization effect due to different constituents of composite. For the simplicity, the isotropic material will be firstly studied. Comparing with the clay matrix, the quartz and calcite can be treated as rigid inclusions. For this reason, the studied COx can be presented by the RVE in Figure 1.

The above complete constitutive modelling with the effects of localization is now applied to describe the macroscopic performance of this claystone with different material compositions and different confining pressures. The porosity is taken $f = 0.25$ as an average value for all simulations. The inclusion content ρ varies with depth. The elastic and plastic parameters are chosen as the ones adopted in [50]. For the simplicity, the volume fraction of the localization zone is taken as $\phi = 0.2$. The parameters are summarized in Table 2.

	Solid phase	Inclusion
Elastic	$E_s = 5GPa$	$E_i = 98GPa$
parameters	$\nu_s = 0.33$	$\nu_i = 0.15$
Plastic	$T_0 = 10^{-10}$, $T_m = 0.68$, $b_1 = b_2 = 200$	
parameters	$t_0 = -1.1$, $t_m = 0.3$, $c_0 = c_1 = 15$ Mpa, $b_3 = 90$	

Table 2: Parameters used in the constitutive model for all the simulations.

Using this same set of parameters, numerical simulations are performed in Abaqus with different loading condition ($P_c = 0$, 5 and 10MPa) on different on different samples with

different mineral compositions. Figure 9-a is for a simulation with uniaxial loading, at the depth 466.8m and the corresponding ρ = 49%. Triaxial compression tests are studied in Figures 9-b and c for Pc = 5 MPa and in Figures 9-d, e and f for Pc = 10 MPa. The inclusion content in these numerical simulations are very different, changes from 40% to 56%. Generally, the model's predictions coincide well with the experimental results. With the consideration of the localization zone, the material strength is well described, especially the mechanical response after the peak point. The influence of microstructural information (f, ρ, α) on the overall response is explicitly considered in this multiscale constitutive modelling.

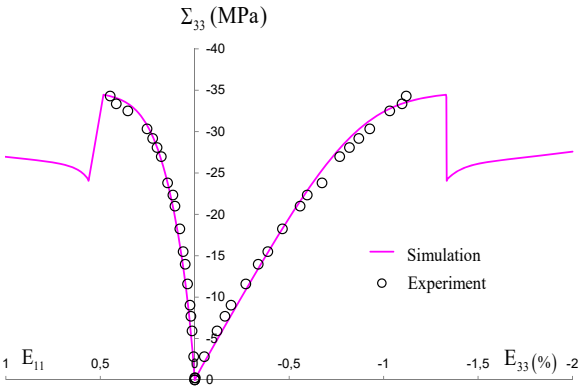

(a) Depth: 466.8m, ρ = 49%, Pc=0Mpa

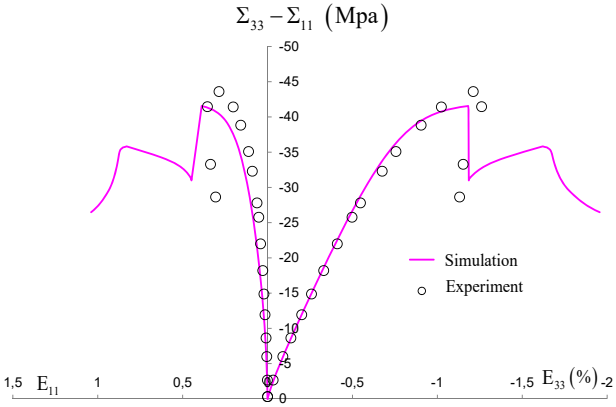

(b) Depth: 469.0m, ρ = 56%, Pc=5Mpa

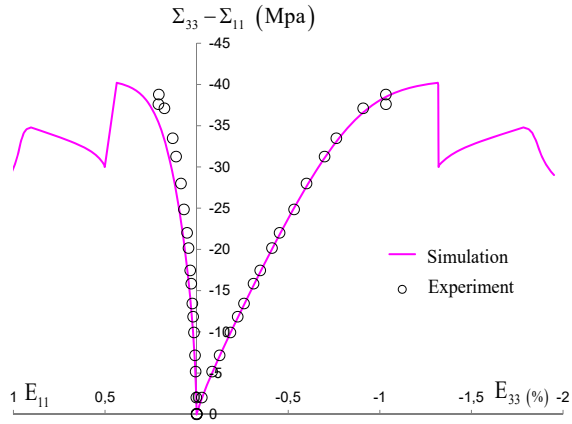

(c) Depth: 451.5m, ρ = 51%, Pc=5Mpa

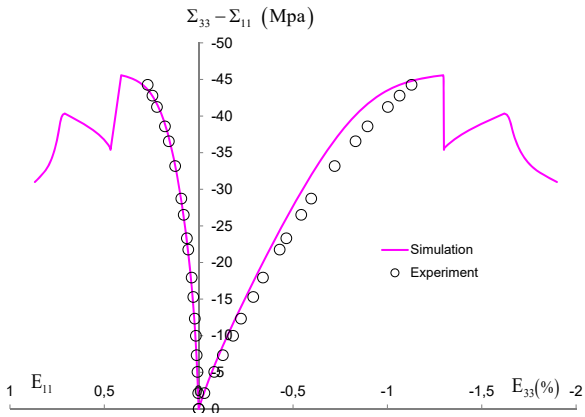

(d) Depth: 451.4m, ρ = 53%, Pc=10Mpa

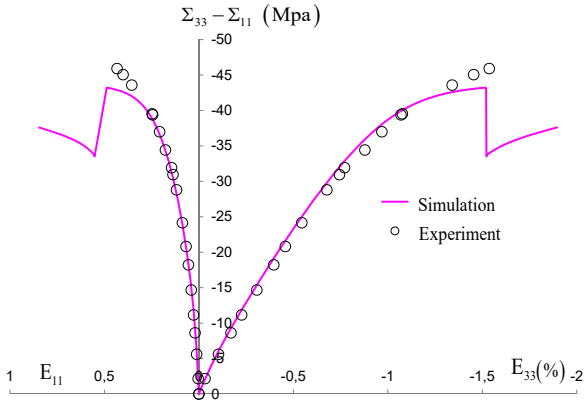

(e) Depth: 469.1m, ρ = 45%, Pc=10Mpa

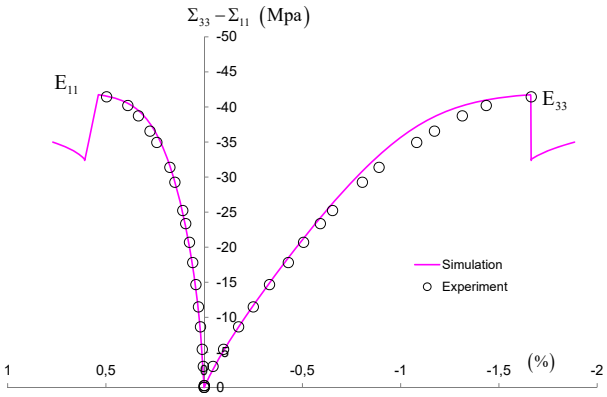

(f) Depth: 482.2m, ρ = 40%, Pc=10Mpa

Figure 9: Model's predictions and experimental results with different composition and different confining pressures

The evolutions of porosity for these compression tests at different depthes and different confining pressures are illustrated in Figure 10. One can see that the variations of f inside the localization zone (dashed lines) are totally different with the outside one (solid lines). Due to the localization, the inside porosity becomes much smaller because of the compaction.

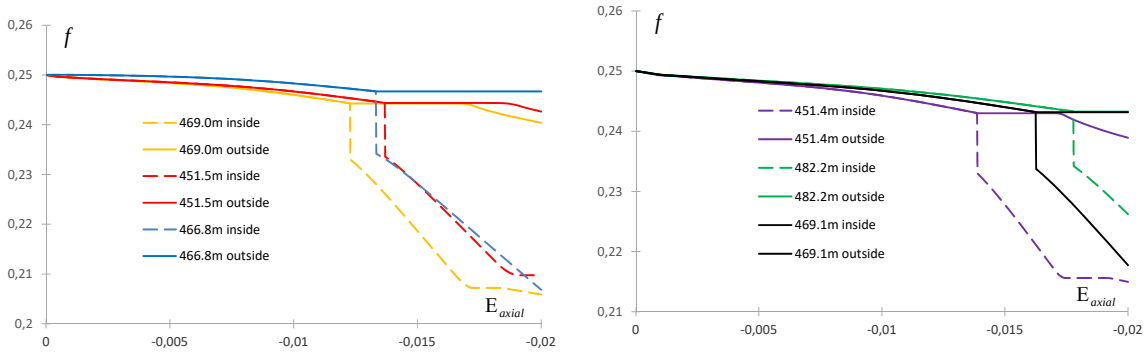

(a) Different ρ for Pc=0 and 5 Mpa

(b) Different ρ for Pc=10 Mpa

Figure 10: Evolutions of porosity in the compression tests at different depthes and different confining pressures.

6. Conclusion

By combining nonlinear homogenization technique and localization analysis, we have developed a new enhanced micro-macro constitutive model with localization analysis for heterogeneous materials with micro-porosity and meso-grains. Compared with existing models, this enhanced multiscale constitutive modelling not only considers the influences of microstructural information on the overall mechanical behaviors of heterogeneous materials, but also captures the onset of localized failure and the post localization behavior. The localization analysis is made at the constitutive level. This makes it very easy for engineering applications. According to the results obtained, the localization behavior is strongly affected by the volume fraction of pores and grains. The local material softening rule has an important influence on the onset point of localization. Further, the proposed enhanced model with localization analysis is well able to predict the overall response of COx claystone in both pre- and post-localization regimes. Therefore, this proposed model gives a fundamental tool for the numerical study of localized damaged and fractured zones around underground

structures.

Acknowledgements

This study was jointly supported by the Programme B18019 of Discipline Expertise to Universities MOE & MST and the National Key RD Program of China (Grant No. 2017YFC1501100).

References

[1] Abou-Chakra Guery, A., Cormery, F., Shao, J. F., Kondo, D., 2008. A micromechanical model of elastoplastic and damage behavior of a cohesive geomaterial. Int.J.Solids Struct 45(5), 1406–1429.

[2] Alam, M. M., Borre, M., Fabricius, I., Hedegaard, K., Røgen, B., Hossain, Z., Krogsbøll, A., 2010. Biot's coefficient as an indicator of strength and porosity reduction: Calcareous sediments from kerguelen plateau. Journal of Petroleum Science and Engineering 70, 282–297.

[3] Armand, G., Conil, N., Talandier, J., Seyedi, D., 2017. Fundamental aspects of the hydromechanical behaviour of callovo- oxfordian claystone: From experimental studies to model calibration and validation. Computers and Geotechnics 85, 277–286.

[4] Barthélémy, J.-F., Dormieux, L., 2003. Détermination du critère de rupture macroscopique d'un milieu poreux par homogénéisation non linéaire. C. R. Mecanique 331, 271–276.

[5] Barthélémy, J. F., Dormieux, L., 2004. A micromechanical approach to the strength criterion of drucker-prager materials reinforced by rigid inclusions. International Journal for Numerical and Analytical Methods in Geomechanics 28, 565–582.

[6] Bignonnet, F., Dormieux, L., Lemarchand, E., 2015. Strength of a matrix with elliptic criterion reinforced by rigid inclusions with imperfect interfaces. European Journal of Mechanics - A/Solids 52, 95 – 106.

[7] Brach, S., Dormieux, L., Kondo, D., Vairo, G., 2017. Nanoporous materials with a general isotropic plastic matrix: Exact limit state under isotropic loadings. International Journal of Plasticity 89, 1–28.

[8] Chiarelli, A. S., 2000. Etude expérimentale et modélisation du comportement mécanique de l'argilite de l'est. Phd, thesis, Université de Lille 1, France.

[9] Chiarelli, A. S., Shao, J. F., Hoteil, N., 2003. Modeling of elastoplastic dammage behavior of a claystone. Int.J.Plasticity 19, 23–45.

[10] De Gennaro, V., Delage, P., Priol, G., Collin, F., Cui, Y., 2004. On the collapse behaviour of oil reservoir chalk. Géotechnique 54(6), 415–420.

[11] Durban, D., Cohen, T., Hollander, Y., 2010. Plastic response ofporous solids with pressure sensitive matrix. Mechanics Research Communications 37, 636–641.

[12] Fritzen, F., Forest, S., Böhlke, T., Kondo, D., Kanit, T., 2012. Computational homogenization of elasto-plastic porous metals. International Journal of Plasticity 29, 102–119.

[13] Garajeu, M., Suquet, P., 1997. Effective properties of porous ideally plastic or viscoplastic materials containing rigid particles. J. Mech. Phys. Solids 45, 873–902.

[14] Gologanu, M., Leblond, J., Devaux, J., 1993. Approximate models for ductile metals containing non-spherical voids–cas of axisymmetric prolate ellipsoidal cavities. J.Mech.Phys.Solids 41(11), 1723–1754.

[15] Gologanu, M., Leblond, J. B., Devaux, J., 1994. Approximate models for ductile metals containing non-spherical voids–cas of axisymmetric oblate ellipsoidal cavities. ASME J.Eng. Mat. Tech. 116, 290–297.

[16] Guo, T., Faleskog, J., Shih, C., 2008. Continuum modeling of a porous solid with pressure sensitive dilatant matrix. J. Mech. Phys. Solids 56, 2188–2212.

[17] Gurson, A., 1977. Continuum theory of ductile rupture by void nucleation and growth: part1-yield criteria and flow rules for porous ductile media. J. Engrg. Mater. Technol. 99, 2–15.

[18] He, Z., Dormieux, L., Kondo, D., 2013. Strength properties of a drucker-prager porous medium reinforced by rigid particles. International Journal of Plasticity 51, 218 – 240.

[19] Homand, S., Shao, J., 2000. Mechanical behavior of a porous chalk and water/chalk interaction. part i: Experimental study. Oil Gas Sci. Technol. 55(6), 591–598.

[20] Hoxha, D., Giraud, A., Homand, F., Auvray, C., 2007. Saturated and unsaturated behaviour modelling of meuse haute marne argillite. International Journal of Plasticity 23(5), 733–766.

[21] Jeong, H., 2002. A new yield function and a hydrostatic stress-controlled model for porous solids with pressure-sensitive matrices. Int. J. Solids Struct. 39, 1385–1403.

[22] Keralavarma, S., Benzerga, A., 2010. A constitutive model for plastically anisotropic solids with non-spherical voids. Journal of the Mechanics and Physics of Solids 58, 874–901.

[23] Lee, J., Oung, J., 2000. Yield functions and flow rules for porous pressure-dependent strain-hardening polymeric materials. J.Appl.Mech. 67, 288–297.

[24] Maghous, S., Dormieux, L., Barthèlèmy, J., 2009. Micromechanical approach to the strength properties of frictional geomaterials. European Journal of Mechanics A/Solid 28, 179–188.

[25] Monchiet, V., Bonnet, G., 2013. A Gurson-type model accounting for void size effects. International Journal of Solids and Structures 50, 320–327.

[26] Monchiet, V., Cazacu, O., Charkaluk, E., Kondo, D., 2008. Macroscopic yield criteria for plastic anisotropic materials containing spheroidal voids. International Journal of Plasticity 24, 1158–1189.

[27] Monchiet, V., Charkaluk, E., Kondo, D., 2014. Macroscopic yield criteria for ductile materials containing spheroidal voids: An eshelby-like velocity fields approach. Mechanics of Materials 72, 1–18.

[28] Monchiet, V., Kondo, D., 2012. Exact solution of a plastic hollow sphere with a mises-schleicher matrix. International Journal of Engineering Sciences 51, 168–178.

[29] Monchiet, V., Kondo, D., 2013. Combined voids size and shape effects on the macroscopic criterion of ductile nanoporous materials. International Journal of Plasticity 43, 20–41.

[30] Mori, T., Tanaka, K., 1973. Average stress in a matrix and average elastic energy of materials with misfitting inclusions. Acta Metall.Mater 42(7), 597–629.

[31] Neilsen M.K., a. S. H., 1993. Bifurcations in elastic-plastic materials. Int J Solids Struct 30, 521–544.

[32] Nguyen, C. T., Nguyen, G. D., Das, A., Bui, H. H., 2017. Constitutive modelling of progressive localised failure in porous sandstones under shearing at high confining pressures. International Journal of Rock Mechanics and Mining Sciences 93, 179 – 195.

[33] Nguyen, G. D., Nguyen, C. T., Bui, H. H., Nguyen, V. P., 2016. Constitutive modelling of compaction localisation in porous sandstones. International Journal of Rock Mechanics and Mining Sciences 83, 57 – 72.

[34] Nguyen, G. D., Nguyen, C. T., Nguyen, V. P., Bui, H. H., Shen, L., 2016. A size-dependent constitutive modelling framework for localised failure analysis. Computational Mechanics 58 (2), 257–280.

[35] Niandou, H., Shao, J., Henry, J., Fourmaintraux, D., 1997. Laboratory investigation of the mechanical behaviour of tournemire shale. Int. J. Rock Mech. Min. Sci. 34, 3–16.

[36] Ottosen, N. S., Runesson, K., 1991. Properties of discontinuous bifurcation solutions in elasto-plasticity. International Journal of Solids and Structures 27 (4), 401 – 421.

[37] Papamichos, E., Brignoli, M., Santarelli, F., 1997. An experimental and theoretical study partially saturated collapsible rock. Int. J. Mech. Cohesive-Frictional Mater. 2, 251–278.

[38] Qi, M., Giraud, A., Colliat, J., Shao, J., 2016. A numerical damage model for initially anisotropic materials. International Journal of Solids and Structures 100-101, 245 – 256.

[39] Qi, M., Shao, J., Giraud, A., Zhu, Q., Colliat, J., 2016. Damage and plastic friction in initially anisotropic quasi brittle materials. International Journal of Plasticity 82, 260 – 282.

[40] Robinet, J. C., 2008. Mineralogie, porosite et diffusion des solutes dans l'argilite du callovo-oxfordien de bure (meuse/haute-marne, france) de l'echelle centimetrique a micrometrique. Phd, thesis, Université de poitiers, France.

[41] Schroeder, C., 2003. Du coccolithe au réservoir pétrolier ; approche phénoménologique du comportement mécanique de la craie en vue de sa modélisation à différentes échelles. Phd, thesis, University of Liège.

[42] Shao, J., Jia, Y., Kondo, D., Chiarelli, A., 2006. A coupled elastoplastic damage model for semi-brittle materials and extension to unsaturated conditions. Mechanics of Materials 38, 218–232.

[43] Shen, W., 2011. Modelisations micro-macro du comportement mecanique des materiaux poreux ductiles : application à l'argilite du callovo-oxfordien. Phd, thesis, University of Lille I, France.

[44] Shen, W., He, Z., Dormieux, L., Kondo, D., 2014. Effective strength of saturated double porous media with a drucker-prager solid phase. Int. J. Numer. Anal. Meth. Geomech. 38, 281–296.

[45] Shen, W., Kondo, D., Dormieux, L., Shao, J., 2013. A closed-form three scale model for ductile rocks with a plastically compressible porous matrix. Mechanics of Materials 59, 73–86.

[46] Shen, W., Lin, J., Zhu, Q., Monchiet, V., Kondo, D., 2011. Macroscopic yield criterion for ductile materials containing randomly oriented spheroidal cavities. International Journal of Damage Mechanics 20, 1198–1216.

[47] Shen, W., Shao, J., Dormieux, L., Kondo, D., 2012. Approximate criteria for ductile porous materials having a Green type matrix: Application to double porous media. Computational Materials Science 62, 189–194.

[48] Shen, W., Shao, J., Kondo, D., Gatmiri, B., 2012. A micro-macro model for clayey rocks with a plastic compressible porous matrix. International Journal of Plasticity 36, 64–85.

[49] Shen, W., Shao, J., Liu, Z., Oueslati, A., Saxcé, G. D., 2019. Evaluation and improvement of macroscopic yield criteria of porous media having a drucker-prager matrix. International Journal of Plasticity, in press.

[50] Shen, W. Q., Kondo, D., Dormieux, L., Shao, J. F., 2013. A closed-form three scale model for ductile rocks with a plastically compressible porous matrix. Mechanics of Materials 59, 73–86.

[51] Shen, W. Q., Lanoye, E., Dormieux, L., Kondo, D., 2014. Homogenization of saturated double porous media with eshelby-like velocity field. Acta Geophysica. 62(5), 1146–1162.

[52] Shen, W. Q., Pastor, F., Kondo, D., 2013. Improved criteria for ductile porous materials having a green type matrix by using eshelby-like velocity fields. Theoretical and Applied Fracture Mechanics 67-68, 14–21.

[53] Shen, W. Q., Shao, J. F., 2016. An incremental micro-macro model for porous geomaterials with double porosity and inclusion. International Journal of Plasticity 83, 37–54.

[54] Shen, W. Q., Shao, J. F., 2017. A micro-mechanics-based elastic-plastic model for porous rocks: applications to sandstone and chalk. Acta Geotechnica 13, 329–340.

[55] Shen, W. Q., Shao, J. F., Kondo, D., 2017. Macroscopic criteria for green type porous materials with spheroidal voids: application to double porous materials. Int. J. Numer. Anal. Meth. Geomech. 41, 1453–1473.

[56] Shen, W. Q., Shao, J. F., Kondo, D., De Saxce, G., 2015. A new macroscopic criterion of porous materials with a mises-schleicher compressible matrix. European Journal of Mechanics A/Solids 49, 531–538.

[57] Shen, W. Q., Zhang, J., Shao, J. F., Kondo, D., 2017. Approximate macroscopic yield criteria for drucker-prager type solids with spheroidal voids. International Journal of Plasticity 99, 221–247.

[58] Vincent, P.-G., Monerie, Y., P., S., 2008. Ductile damage of porous materials with two populations of voids. C.R.Mecanique 336, 245–259.

[59] Vincent, P.-G., Monerie, Y., P., S., 2009. Porous materials with two populations of voids under internal pressure: I. instantaneous constitutive relations. Int J Solids Struct 46, 480–506.